THE ASTRONOMICAL JOURNAL VOLUME 107, NUMBER 6 JUNE 1994

OPTICAL OBSERVATIONS OF NGC 2915: A NEARBY BLUE COMPACT DWARF GALAXY

G. R. MEURER[1]

Département de Physique and Observatoire du Mont Mégantic, Université de Montréal, Montreal, PQ H3C 3J7 and Space Telescope Science Institute 3700 San Martin Drive, Baltimore, Maryland 21218
Electronic mail: meurer@poutine.pha.jhu.edu

G. MACKIE[2,3]

Harvard-Smithsonian Center for Astrophysics, 60 Garden Street Cambridge, Massachusetts 02138
Electronic mail: mackie@bunyip.harvard.edu

C. CARIGNAN

Département de Physique and Observatoire du Mont Mégantic, Université de Montréal, Montreal, PQ H3C 3J7
Electronic mail: claude@astro.umontreal.ca

Received 1993 August 23; revised 1994 February 7

ABSTRACT

This paper presents B and R band CCD images and medium resolution spectroscopy of NGC 2915, a relatively isolated BCD (blue compact dwarf) galaxy at a distance of ~5 Mpc. NGC 2915 contains two stellar populations: a high surface brightness blue core population and a red diffuse population. The core population contains all of the H II, and numerous embedded objects. It is the locus of current high mass star formation. The brightest embedded objects are likely to be young ionizing clusters, while many of the fainter objects are likely to be individual supergiant stars with masses up to $\sim 25 \mathscr{M}_{\odot}$, or blends of a few such stars. Curious aligned structures on the SE side of the galaxy are seen and their nature discussed. The spectrum of the core is dominated by bright narrow emission lines like that of a high excitation and low metallicity (less than half solar) H II region. The continuum is flat, with Balmer and Ca II features seen in absorption. The velocity of the Ca II features suggest contamination by galactic interstellar absorption. There is a significant velocity gradient in the spectra, probably indicative of rotation. Outside of its core, NGC 2915 resembles a dE (dwarf elliptical) galaxy, in that it has an exponential surface bightness profile, is red $[(B-R)_0=1.65]$, and has a low extrapolated central surface brightness $[B(0)_c=22.44]$. NGC 2915's properties are compared with other BCDs, concentrating on two morphologically similar BCDs that are near enough to resolve into stars: NGC 1705 and NGC 5253. It is noted that the presence of winds in BCDs invalidates closed box chemical evolution models and the remaining constraints on star formation duration are relatively weak. Some BCDs, including NGC 2915, may be able to maintain their present star formation rate for Gyr time scales. This suggests that the overall evolution of these BCDs may be much slower than the ~10 Myr burst time scales commonly quoted. However, shortly after the formation of a massive $(10^6 \mathscr{M}_{\odot})$ cluster a BCD will have all the properties of strong starburst galaxy.

1. INTRODUCTION

The selection criteria used by Thuan & Martin (1981, hereafter referred to as TM) to isolate blue compact dwarf (BCD) galaxies are (1) low luminosity ($M_B \gtrsim -18$); (2) a blue spectrum with narrow emission lines; and (3) a small diameter ($\lesssim 1$ Kpc). Since the size constraint is expressed in absolute terms, it should be distance independent. However, in reality BCDs are preferentially selected for compact angular size due to the methods used in the original surveys from which BCDs are drawn. For example, searches for UV bright objects using either objective prisms (e.g., Markarian 1967) or multiple-exposure plates (Haro 1956) work best for angularly small objects. In the former case, it is difficult to determine the spectral properties of objects whose size is on the order of the length of the spectrum. In the latter case, UV bright point sources are easy to distinguish because the U image is noticeably enlarged with respect to the other images. This size difference is harder to distinguish for extended objects.

Selecting for angular compactness means selecting preferentially distant objects. However, to determine the anatomy of BCDs (e.g., the contents and distribution of stars gas and dark matter), the nearest such objects should be studied. This paper focuses on NGC 2915 (distance, $D \approx 5$ Mpc). From the observations presented here, it is clear that it is a BCD. It easily passes TM's first two criteria. Their size criterion is fairly loose and follow-up observations indicate that it applies to an isophote of fairly high surface brightness (Loose & Thuan 1985). Compared to other BCDs NGC 2915 has a

[1]Present address: Department of Physics and Astronomy, The Johns Hopkins University, 34th and Charles Streets, Baltimore, MD 21218.
[2]Former address: Space Astronomy Laboratory, University of Wisconsin-Madison.
[3]Visiting Astronomer at the Cerro Tololo Inter-American Observatory of the National Optical Astronomy Observatories, which is operated by Associated Universities for Research in Astronomy, Inc., under contract to the National Science Foundation.

 0004-6256/94/107(6)/2021/15/$0.90

normal size, no matter what "ruler" is used. For example, consider the diameter of the core population (Sec. *4.1*) which is 1.8 Kpc for NGC 2915 and 3.2 Kpc for RMB 46 [Bothun *et al.* (1986), with $D_{\rm Virgo}$=21.9 Mpc]. Furthermore, NGC 2915 has a high central surface brightness, $\mu_{B,0}$=20.2 mag arcsec^{-2}. This means that it would not normally be classified as dwarf irregular (dI) nor dwarf elliptical (dE) (which are usually selected by the criterion $\mu_0 \gtrsim 22$ mag arcsec^{-2}).

A galaxy with a very similar morphology to NGC 2915 is NGC 5253. This galaxy was studied in detail by Caldwell & Phillips (1989, hereafter referred to as CP), and had its distance, D=4.1 Mpc, accurately measured by Sandage *et al.* (1994) using Cepheid variables. Using the same type of reasoning as above, it is clear that it is also a BCD. Similarly, Meurer *et al.* (1992, hereafter referred to as MFDC) determined that NGC 1705 is a BCD. NGC 1705, NGC 2915, and NGC 5253, are not usually recognized as BCDs. Instead they are classified as "amorphous" by Sandage & Brucato (1979) or Gallagher & Hunter (1987). By applying TM's luminosity constraint to select the dwarf amorphous galaxies (dAg), one isolates a sample with virtually the same properties as TM's BCDs except they tend to be nearer; 75% (12/16) of the dAgs in the samples of Sandage and Brucato, and Gallagher and Hunter have V_0<1000 km s^{-1}, while only 32% (37/115) of TM's BCDs have such low velocities. Here NGC 1705, NGC 2915, and NGC 5253 will be referred to as dAg/BCDs.[4] This is not meant to imply a morphological distinction from other BCDs, but merely as a convenient way to group BCDs that are also classified as amorphous. The resemblance between NGC 2915 and NGC 5253 is particularly important since it is the basis of the distance estimate for NGC 2915 presented in Sec. *4.3*.

NGC 2915, is a particularly interesting galaxy because: (1) It may be one of the nearest BCDs. Schmidt & Boller (1992) adopt a distance of D=4.1 Mpc based on its radial velocity, V_r, and a linear virgocentric inflow model for the $D(V_r)$ relationship. Unfortunately, this does not provide a very accurate measure of distance. Allowing for average peculiar motions of 90 km s^{-1} (Aaronson *et al.* 1982), and considering the uncertainty in the value of H_0, plausible redshift distances range from 1 to 6 Mpc from this method. It has no group membership which can be used to provide an accurate distance. (2) Its H I properties appear to be that of a much more massive galaxy than seen in the optical; it has a very extended H I distribution and a double horn spectrum (Becker *et al.* 1988) (such profiles are seen in only ~8% of TM's sample). This makes it an ideal candidate for dark matter studies. With this in mind, an H I aperture synthesis study of NGC 2915 has been initiated using the Australia Telescope (Paper II: Meurer *et al.* 1994). One of the goals of that paper is to determine the mass-to-light ratio, and this requires accurate values for quantities best determined in the optical; namely the distance, and the reddening.

NGC 2915 was studied in detail by Sérsic *et al.* (1977, hereafter referred to as SBC). They note the presence of two "ejecta" at either end of the major axis and thus classify it as an explosive Irr II galaxy (Krienke & Hodge 1974). Sérsic & Donzelli (1992, hereafter referred to as SD) update the study of SBC by presenting digitized photographs of NGC 2915 and NGC 5253 (note that east and west should be reversed in SBC's and SD's images of NGC 2915). Both West (1976) and SBC find that NGC 2915 has a strong emission line spectrum. However, SBC claim it has a low excitation H II spectrum whereas West says the spectrum resembles that of extragalactic giant H II regions which usually have high excitation. Neither provides tracings of their spectra. Gallagher & Hunter (1987) provide photometry and note that NGC 2915 has a low potential for interaction. Indeed there are no galaxies listed in the NASA/IPAC Extragalactic Database (NED)[5] within 5° of NGC 2915 with V_r<1000 km s^{-1}. However, there is a low surface brightness object, SGC 0938.1−7623 (Corwin *et al.* 1985), that is 42′ away (projected distance 65 Kpc) and which cannot be ruled out as a companion since its velocity is unknown.

This study presents long slit spectroscopy and CCD images of NGC 2915 with the aims of determining some of its global properties and examining its stellar populations. For quick reference and to preview the results, some important properties of NGC 2915 are listed in Table 1. The reference column notes either the study used as the source or the section where the quantity is discussed in more detail. The first four entries give the position of the galaxy's light peak in equatorial and galactic coordinates. All offset positions in this paper are relative to this position. We adopt the heliocentric radial velocity, V_r, listed by Schmidt & Boller [(1992); the mean of various sources in the literature] which is more accurate but consistent with the value V_r=490±35 km s^{-1}, determined from the spectra presented here. $E(B-V)_f$ is the foreground (galactic) reddening; $E(B-V)_{\rm em}$ is the total reddening applicable to the emission lines; and $E(B-V)$ is the reddening applicable to the broadband and continuum light (it corresponds to A_B=0.60±0.15). Here the extinction law of Rieke & Lebofsky (1985) is adopted. The total apparent B magnitude is m_{B_T}, determined by extrapolating the observed surface brightness profile to account for the portion of the galaxy outside of the CCD images. The corresponding absolute magnitude is given by M_{B_T}. The total color of the galaxy $(B-R)_{T,0}$, was derived in the same manner. The extrapolated central face-on reddening corrected surface brightness is $B(0)_c$ (following Freeman 1970). The Holmberg diameter, $d_{\rm Ho}$, is the major axis diameter of the isophote with $\mu_{B,0}$=26.6 mag arcsec^{-2}. The upper limit to the oxygen abundance, 12+log(O/H), was determined from the ratios [O III]5007/Hβ and ([O II]3727 +[O III]4959,5007)/Hβ using the line fluxes presented in Sec. 3 and Figs. 8 and 10 of Dopita & Evans (1986). This limit corresponds to about half solar abundance. The reddening corrected Hα flux, $F_{0,{\rm H}\alpha}$ was determined from the narrowband CCD frames of A. Marlowe and T. Heckman who kindly made their data and measurements available to us before publication (Marlowe *et al.* 1994). Their data agree with the Hα flux measurements of Gallagher & Hunter

[4]Other dAgs that are likely to be BCDs are NGC 1569, and NGC 3077.

[5]The NASA/IPAC Extragalactic Database (NED) is operated by the Jet Propulsion Laboratory, California Institute of Technology, under contract with the National Aeronautics and Space Administration.

TABLE 1. Properties of NGC 2915.

Quantity	value	Reference
RA (J2000)	$9^h\ 26^m\ 11\overset{s}{.}83$	section 1
Dec (J2000)	$-76°\ 37'\ 35\overset{''}{.}8$	section 1
l^{II}	$291\overset{\circ}{.}97$	
b^{II}	$-18\overset{\circ}{.}36$	
V_r	468 ± 5 km s^{-1}	Schmidt and Boller (1992)
D	5.3 ± 1.6 Mpc	section 4.3
classification	BCD	section 1
$E(B-V)_f$	0.13 ± 0.02	Burstein and Heiles (1984)
$E(B-V)_{em}$	0.44 ± 0.15	section 4.3
$E(B-V)$	0.15 ± 0.05	section 4.3
m_{B_T}	13.34	section 1
M_{B_T}	-15.90	section 1
$(B-R)_{T,0}$	1.40	section 1
$B(0)_c$	22.44 mag arcsec^{-2}	section 2
$d_{\rm Ho}$	$3.8' = 5.86$ Kpc	section 1
$12 + \log({\rm O/H})$	$\lesssim 8.5$	section 1
$F_{0,{\rm H}\alpha}$	1.9×10^{-12} erg cm^{-2} s^{-1}	section 1
$M_{\rm HI}$	$6.8 \times 10^8\ M_\odot$	Becker *et al.* (1988)
$M_{\rm HI}/L_B$	$1.9\ M_\odot/L_{B,\odot}$	
$F_{\rm IR}$	5.0×10^{-11} erg cm^{-2} s^{-1}	Schmidt and Boller (1992)
$M_{\rm Dust}$	$10500\ M_\odot$	Schmidt and Boller (1992)

(1987). $\mathscr{M}_{\rm H\,I}$ is the neutral hydrogen mass. The far infrared flux, $F_{\rm IR}$, and dust mass, $\mathscr{M}_{\rm Dust}$, were derived from fluxes in the *IRAS Point Source Catalog* (1988) by Schmidt & Boller (1992).

The rest of this paper is divided as follows. The imaging data, its reduction and analysis, are presented in Sec. 2. Likewise, the spectroscopic data, its reduction and analysis, are presented in Sec. 3. The properties of NGC 2915 are discussed in Sec. 4. Section 5 compares the properties of the three dAg/BCDs and other BCDs and discusses scenarios for their evolution. Conclusions and suggestions for future research are presented in Sec. 6.

2. IMAGING

Unguided prime focus images of NGC 2915 were obtained with the 3.9 m Anglo-Australian Telescope (AAT) using Johnson B (200 s, 150 s) and Kron-Cousins R (2×40 s, 2×120 s) filters. The images were obtained on 1990 December 17 at an airmass of 1.46 using the 350×512 pixel RCA CCD chip which has a projected pixel size of 0.49″, and a readout noise of 37 electrons. Effective seeing values ranged from 1.6″ for the short R exposures to 2.1″ for one of the long R exposures.

Data reduction (mostly done with the *Image Reduction and Analysis Facility (IRAF)* package) included bias subtraction, a slight nonlinearity correction following Robinson *et al.* (1989), and flatfielding using twilight flats. Fringe frame subtraction was not required on any of the frames.

TABLE 2. Comparison with published photometry.

Ap. (″)	V (photo-electric	$U-B$	$B-V$	$V-R$)	B (CCD)	$B-R$	ΔB (CCD − pe)	ΔR	ref
19.0	14.09	−0.13	0.52		14.57	0.99	−0.04		A
22.0	13.56	−0.33	0.48		14.40	1.02	0.36		B
29.0	13.56			0.45	14.10	1.07		−0.08	C
33.8	13.37	−0.13	0.60		13.95	1.10	−0.02		D
37.9	13.31	0.05	0.48		13.86	1.12	0.07		A
60.0	12.78	−0.32	0.62		13.55	1.20	0.15		B
90.0	12.76	−0.25	0.53		13.37	1.26	0.08		B
95.1	12.71	−0.25	0.58		13.35	1.27	0.06		A

References.—(A) Longo & de Vaucouleurs (1983) as quoted by Laubers & Sadler (1984); (B) SBC; (C) Gallagher & Hunter (1987); (D) Wegner (1979) as quoted by Lauberts

Pixel values affected by hot spots, cosmic rays, and other image defects were replaced with a locally fitted surface plus artificial noise. The sky level and its uncertainty were determined from the mode of values in 40×40 boxes at the eastern and western edges of the frames, well outside the body of the galaxy. The frames were shifted to a common origin and then summed to make total B and R images. An image made by adding the two 40 s R exposures (thus preserving their higher resolution) was also analyzed.

The photometric calibration to the system of Graham (1982) was determined using observations of ten standard stars in each band. $(B-R)$ color terms were determined from archival data taken with the same chip and filters. These terms were adopted in the calibration of the night's data in which a zero-point and extinction term were determined for each band. The standard deviation of the residuals was 0.012 mag in each band, which is adopted as the zero-point uncertainty. To test the calibration, synthetic aperture photometry was performed on NGC 2915 using aperture sizes corresponding to those of published photoelectric measurements. The results are presented in Table 2. In the B band the mean difference (CCD−photoelectric) is 0.09 mag. Excluding the photometry of SBC, which has the most discrepant B magnitudes (especially in the 22″ aperture), the mean difference becomes 0.02 mag. The remaining individual differences are on the order of typical external errors in photoelectric measurements (Wegner 1979).

The reduced R image is shown in Fig. 1 (Plate 130). The most apparent feature is the irregular inner structure of numerous embedded objects. In comparison the outer isophotes are relatively smooth. The image analysis is therefore directed at three goals: (1) obtaining photometry of the embedded objects, (2) determining the parameters of the isophotes, and (3) measuring the surface brightness and color profiles.

To perform photometry of the embedded objects requires that the smooth and "lumpy" structures be separated. Photometry is then performed on the lumpy images which should contain only the foreground and background sources, and the embedded objects. Figure 2 (Plate 131) shows vari-

ous versions of the lumpy images. As a first iteration the separation was done in a manner similar to that done for NGC 1705 by MFDC. The smooth image was made by interactively removing all compact sources (in the same manner that the cosmic rays were removed) and then smoothing the data with a 5×5 pixel median filter. This filter removes any peaks in the data missed by interactively "zapping" objects. The lumpy image is then the original image minus the smooth image.

Figure 2(a) is the resultant R lumpy image. This first iteration is not satisfactory. Because of the crowding in the center, a small aperture is required when removing the central sources. Thus the wings of the sources are not adequately removed, resulting in negative halos around the central sources in the lumpy image. Therefore an iterative approach was adopted to simultaneously perform the crowded field photometry and improve the smooth–lumpy separation, using tools mainly contained in the DAOPHOT package of Stetson (1987) as implemented in IRAF. The method is similar to that of Deharveng *et al.* (1992). It assumes all objects in the lumpy image can be modeled as the sum of point sources. The point spread function of each frame is determined from uncrowded stars well away from the galaxy's center. The ALLSTAR program in DAOPHOT is run on the lumpy image, adding and deleting sources as necessary to obtain the best looking residual map. The central residuals (a ~70″×50″ patch) are isolated and median filtered (using a 7×7 box for the first two iterations and a 5×5 box for the last iteration). The resultant image is added to the smooth image and subtracted from the lumpy image to get improved versions of both. Three such improvements adequately restored the wings to the embedded sources and therefore the iterations were stopped. Figure 2(b) shows the final R lumpy image. The magnitudes converged by the last iteration for about 70% of the central objects. Further iterations were not attempted because this procedure can transfer lumpy structure to the smooth image and mask the nature of the embedded objects. As an example, object 129 initially appears to be a background galaxy, but this method puts its halo into the smooth image and makes its core look like a point source in the lumpy image.

The resulting measurements of the total B and R images are given in Table 3. Only objects within a circular radius of 30″ (770 pc) of the peak in the light distribution are listed. These objects are identified in Fig. 3. The first column gives an identification number for the object. The first 12 objects are those within 10″ of the center. The second and third columns give the east and north offset position relative to the position noted in Table 1. The coordinate system was tied to six SAO stars via six relatively bright stars visible on both the CCD images and a UKST IIIa-J Survey film. Positions on the survey film were measured with the AAO PDS microdensitometer. Final absolute position errors are ±0.6″ and relative errors are likely to be at most 0.3″. The apparent magnitude and color of the objects are given in the fourth and fifth columns. Their errors are the measurement errors given by the ALLSTAR package. In addition there is a systematic uncertainty of 0.02 mag in each band which has not been included. This is comprised of the uncertainties in the photometric zero-points and the aperture corrections. The measurement errors should be considered lower limits for extended objects which are flagged in the final column. An object was flagged for one or more of four reasons: (1) it

TABLE 3. Embedded object photometry.

id	Δα (″)	Δδ (″)	R	$B-R$	notes
1	−0.36	−0.01	18.26 ± 0.04	0.57 ± 0.06	m2
2	1.85	−4.71	18.45 ± 0.03	0.79 ± 0.13	m3
3	4.16	−2.95	18.77 ± 0.03	0.78 ± 0.07	m3
4	−4.17	3.64	19.25 ± 0.05	0.55 ± 0.07	m3
5	−2.41	0.53	19.34 ± 0.02	···	e
6	−1.49	−5.99	19.94 ± 0.03	1.29 ± 0.05	
7	−1.60	3.75	20.20 ± 0.04	0.75 ± 0.10	
8	−1.07	7.07	21.45 ± 0.08	0.27 ± 0.10	c,e
9	2.46	2.81	21.73 ± 0.15	0.10 ± 0.20	e,d
10	6.59	4.18	22.24 ± 0.09	···	e,d
11	3.06	−8.71	23.02 ± 0.25	0.17 ± 0.35	
12	−7.88	−0.59	23.05 ± 0.28	1.75 ± 0.55	c
101	25.96	4.79	18.93 ± 0.00	1.55 ± 0.01	
102	24.52	−12.30	22.39 ± 0.13	···	
103	23.56	−17.92	21.25 ± 0.04	2.16 ± 0.09	m2
104	21.67	−12.31	21.01 ± 0.02	···	
105	19.29	6.31	22.66 ± 0.09	···	
106	18.57	−9.18	22.41 ± 0.08	···	
107	16.25	18.85	21.50 ± 0.03	···	
108	16.09	1.65	23.51 ± 0.17	···	
109	15.88	−6.89	22.01 ± 0.09	0.73 ± 0.15	c,e
110	14.38	−17.28	19.16 ± 0.02	0.64 ± 0.05	m4
111	14.39	−11.17	21.77 ± 0.08	1.04 ± 0.13	e,d
112	13.57	−5.58	21.32 ± 0.05	···	e
113	13.31	19.21	22.80 ± 0.06	0.19 ± 0.10	
114	12.70	−0.71	22.82 ± 0.17	0.05 ± 0.24	c,e
115	11.53	−3.18	22.48 ± 0.10	0.12 ± 0.16	c,d
116	10.16	−13.43	20.37 ± 0.03	2.06 ± 0.10	e,d
117	9.70	−7.31	20.01 ± 0.02	1.05 ± 0.04	e
118	6.65	−10.82	19.92 ± 0.06	1.76 ± 0.09	m2
119	4.18	16.45	22.87 ± 0.12	···	
120	3.96	−17.68	20.45 ± 0.01	0.86 ± 0.03	
121	3.00	−25.71	22.89 ± 0.14	0.55 ± 0.22	
122	−0.68	11.19	22.13 ± 0.12	···	d
123	−1.56	−26.48	22.90 ± 0.08	0.09 ± 0.13	
124	−2.88	−10.87	23.57 ± 0.19	···	
125	−3.34	11.65	21.67 ± 0.06	0.61 ± 0.10	e
126	−4.70	9.51	22.79 ± 0.14	···	
127	−6.25	27.83	23.47 ± 0.19	0.39 ± 0.32	c
128	−6.55	−9.49	21.59 ± 0.05	···	
129	−7.16	21.69	20.93 ± 0.04	2.02 ± 0.13	e
130	−7.30	11.66	21.60 ± 0.06	···	
131	−8.13	18.35	22.38 ± 0.08	0.86 ± 0.16	
132	−8.31	9.15	22.83 ± 0.13	···	
133	−11.23	−13.95	21.31 ± 0.02	1.59 ± 0.06	
134	−11.70	4.83	21.49 ± 0.04	2.06 ± 0.14	c
135	−11.84	11.41	21.84 ± 0.05	0.81 ± 0.09	e
136	−11.83	16.47	23.52 ± 0.18	−0.50 ± 0.24	
137	−13.06	−3.04	21.90 ± 0.04	···	
138	−14.86	−19.11	21.18 ± 0.02	2.04 ± 0.12	
139	−19.75	−8.43	21.61 ± 0.03	···	
140	−30.15	−0.69	22.25 ± 0.06	1.75 ± 0.13	

Note to TABLE 3

Note. Definite or likely nonpoint sources are indicated in the notes column by the following codes: (m) Modeled as multiple point sources, the number indicates the number of components used; (e) appears elongated or extended to the eye; (d) low sharpness parameter returned by ALLSTAR: (c) coordinates differ by $\Delta r>1$ pixel in different frames.

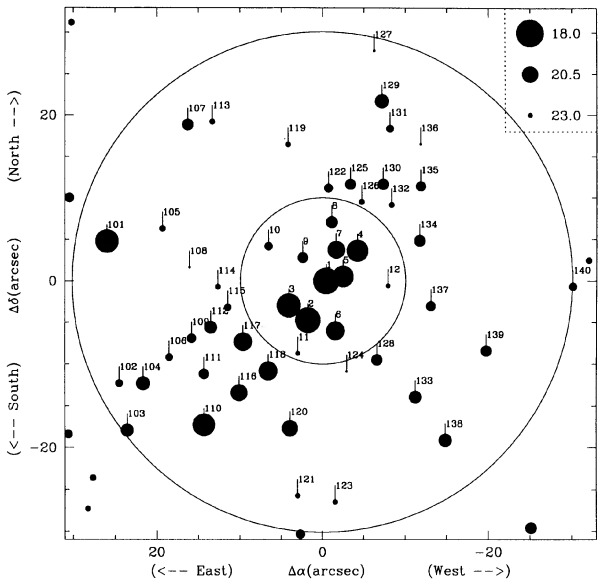

FIG. 3. Finding chart for objects identified in the lumpy image, and with photometry listed in Table 3. The circles have radii of 10″ and 30″. The correspondence between symbol size and R magnitude is given in the upper right of the diagram.

could be modeled as multiple point sources (the photometry of the combined object is reported here); (2) it appeared elongated or distorted to the eye in displayed images; (3) it had a sharpness parameter (Stetson 1987) outside the envelope of the majority of points in the sharpness versus magnitude diagram. (Both 2 and 3 were checked in the original and the final iteration lumpy images); (4) It had positions differing by more than one pixel between the B and R frames. The same procedure was applied to the sum of the two short exposure R frames. No extra objects were found, but this frame was useful in determining which objects are extended.

Isophote parameters in the B and R (and short exposure R) images were measured using a moment analysis method adapted from Ichikawa *et al.* (1986) applied to the first iteration smooth images described above. For a given surface brightness, the zeroth moment of the distribution [see Ichikawa *et al.* (1986) for how the moments are defined] defines the area of the isophote, which yields the semimajor axis length, a, once the axial ratio, a/b, is determined. The first moments yield the center coordinates, X_c, Y_c, of the isophote, and the second moments yield the position angle, ϕ, and a/b. The parameters were determined at quarter magnitude intervals of surface brightness, out to $a \approx 78''$ where the isophotes abut the southern edge of the CCD frame. The results are given in Table 4 and shown in Fig. 4. The isophote parameters follow the same trends in both bands.

Elliptical aperture and annular photometry was performed on images which had the foreground objects removed but left the central lumpy structure intact. The ellipse parameters for each aperture were taken from smooth curves fitted to the moment analysis results (shown as solid lines in Fig. 4). The curves are chosen so that for $a > 78''$ they quickly asymptote

TABLE 4. Moment analysis results.

a_B	$X_{c,B}$	$Y_{c,B}$	ϕ_B	$(a/b)_B$	a_R	$X_{c,R}$	$Y_{c,R}$	ϕ_R	$(a/b)_R$
3.54	0.41	−1.61	−34.2	1.56	5.83	0.98	−2.02	−47.4	2.10
6.35	0.57	−1.57	−43.1	1.88	8.43	1.79	−2.40	−48.1	1.84
8.38	1.15	−1.91	−45.0	1.88	11.83	2.78	−2.89	−50.2	2.03
11.71	2.65	−2.71	−50.2	2.14	13.90	3.34	−2.91	−50.8	1.89
13.26	2.99	−2.83	−50.3	2.02	16.22	3.76	−2.94	−51.2	1.80
15.03	3.38	−2.87	−51.3	1.89	18.66	4.04	−2.79	−49.8	1.73
17.43	3.51	−2.58	−49.4	1.91	21.30	4.26	−2.94	−49.8	1.69
19.58	3.77	−2.41	−47.9	1.84	23.74	4.63	−3.26	−51.4	1.62
21.52	4.10	−2.61	−48.6	1.77	26.25	5.05	−3.36	−52.6	1.55
23.52	4.34	−2.89	−49.9	1.68	29.36	5.36	−3.53	−52.1	1.52
25.87	4.90	−3.10	−51.5	1.64	33.08	5.50	−3.75	−51.6	1.54
28.23	5.23	−3.30	−51.7	1.58	36.98	5.37	−4.25	−51.5	1.57
31.82	5.53	−3.41	−51.0	1.60	42.40	5.60	−4.94	−52.4	1.66
35.06	5.39	−3.57	−51.6	1.61	48.57	6.32	−6.21	−52.2	1.76
38.54	5.31	−3.93	−51.8	1.62	55.08	7.40	−7.45	−52.0	1.84
43.94	5.48	−4.82	−52.2	1.71	61.84	9.14	−8.73	−51.6	1.88
50.50	6.02	−5.88	−52.2	1.83	67.81	10.76	−9.44	−51.8	1.90
55.82	6.67	−6.98	−52.1	1.87	73.12	11.42	−9.23	−51.4	1.87
61.51	8.10	−7.91	−52.2	1.88	77.93	12.13	−8.82	−52.0	1.85
67.21	9.07	−8.12	−52.3	1.91	...	...	...	...	...
73.00	9.70	−7.95	−51.1	1.91	...	...	...	...	...
77.21	9.33	−7.14	−50.9	1.88	...	...	...	...	...

Note. — Units for a, X_c, and Y_c are arcseconds. Units for ϕ are degrees.

to a constant value. The difference in flux between successive apertures yields the surface brightness profile. The resultant extinction corrected surface brightness and color profiles are listed in Table 5 and illustrated in Fig. 5. Figure 5 also shows the surface density of embedded objects as a function of a.

The surface brightness profile is exponential (linear with radius) at large radii. A linear fit was performed to the points with $a > 35''$. The resultant exponential scale lengths are $\alpha_B^{-1} = 25.6''$, and $\alpha_R^{-1} = 25.1''$. The extrapolated central surface brightnesses after correcting for extinction and inclination are $B(0)_c = 22.44$, $R(0)_c = 20.76$ mag arcsec^{-2}.

3. SPECTROSCOPY

Two-dimensional spectroscopy was obtained on 1991 June 7, with the Cassegrain Spectrograph on the CTIO 1.0 m telescope and the 2D-Frutti detector. A 300 lines mm^{-1} grating was employed. The slit had an east-west orientation, and was 4″ wide, resulting in a 7.6 Å resolution. The reduced spectra cover the wavelength range 3510–7006 Å with a pixel size 3.6″×2.32 Å. Two 1800 s exposures of NGC 2915 were obtained, along with various calibration frames.

Data reduction included flatfield division, rectification of the detector S-distortion, wavelength calibration, sky sub-

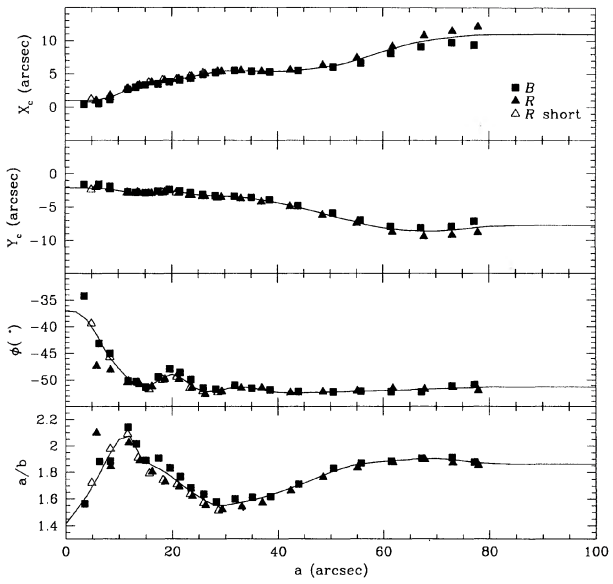

FIG. 4. Moment analysis results. The solid line shows the adopted fit to the parameters as a function of a.

traction and division by a smooth spectrum source. A spectrum of Kopf 27 (Stone 1977), obtained on the same night and at a similar airmass, was used to flux calibrate the data. The rms of the residuals about the adopted fit is 0.04 mag. But relative fluxes are probably only good to ~10% due to the inadequacies in the flatfielding and smooth spectrum source division. One-dimensional spectra were extracted (no weighting) in six apertures; one large aperture for the integrated spectrum, and five adjoining small apertures to search for a velocity gradient along the slit. The aperture positions relative to the distribution of continuum and [O III] 5007 Å light along the slit are shown in Fig. 6. The integrated spectrum is shown in Fig. 7. The top panel shows the complete spectrum, while the lower two panels expand the red and blue ends of the spectrum to show line identifications and the expected positions of lines which have a less than 2σ detection.

The spectrum of NGC 2915 is flat with sharp narrow emission lines and line ratios (especially [O III] 5007 Å/Hβ) that are typical of high excitation H II regions (cf. with Fig. 1 of McCall *et al.* 1985). Although the excitation is not as high as some extreme examples (e.g., I Zw 36; Viallefond & Thuan 1983), we do not concur with SBC that the spectrum has a low excitation, nor can we reproduce their Hα/[O III] 4959+5007 Å flux ratio. In addition to the emission lines, a strong Balmer series and the Ca II H+K lines are seen in absorption. The mean emission line velocity, using Hβ, [O III]4959,5007 Å, and Hα, is V_r=489±35 km s^{-1}. It agrees well with the mean Balmer absorption line velocity, using Hδ, H8 and H9, of V_r=492±37 km s^{-1}. The values of V_r for Ca II K, and the blend Ca II H+Hϵ, 379 and 318 km s^{-1}, respectively, are considerably lower, suggesting that the Ca II lines are contaminated by galactic interstellar absorption.

TABLE 5. Surface photometry.

a	μ_{B_0}	μ_{R_0}	$(B-R)_0$
0.71	19.50	18.62	0.88
2.24	19.46	18.58	0.88
4.12	19.64	18.69	0.95
6.08	19.98	18.95	1.03
8.06	20.21	19.13	1.08
10.05	20.38	19.26	1.12
12.04	20.65	19.48	1.17
14.04	20.93	19.70	1.23
16.03	21.21	19.92	1.28
18.03	21.41	20.10	1.31
20.02	21.64	20.30	1.34
22.07	21.93	20.53	1.41
24.28	22.20	20.76	1.44
26.71	22.48	21.00	1.48
29.38	22.70	21.19	1.51
32.32	22.89	21.34	1.55
35.55	23.15	21.56	1.59
39.11	23.38	21.79	1.60
43.02	23.60	21.99	1.61
47.32	23.78	22.17	1.61
52.05	23.95	22.33	1.62
57.26	24.18	22.53	1.65
62.98	24.42	22.75	1.67
.28	24.70	23.04	1.66
76.21	25.05	23.36	1.69
83.83	25.43	23.75	1.68
92.21	25.79	24.12	1.67
101.40	26.23	24.48	...
111.60	26.47	...	...
122.70	26.97	...	...

Note. — Units for a are arcseconds. Units for μ are mag arcsec^{-2}.

Relative emission line fluxes are presented in Table 6. Most were measured using Gaussian fits to the data, except for [Ne III]3869 Å and [S II]6716+6731 Å which were measured by straight integration. The errors were determined from photon statistics. Relative fluxes, both observed and dereddened, are presented in columns 3 and 4, respectively.

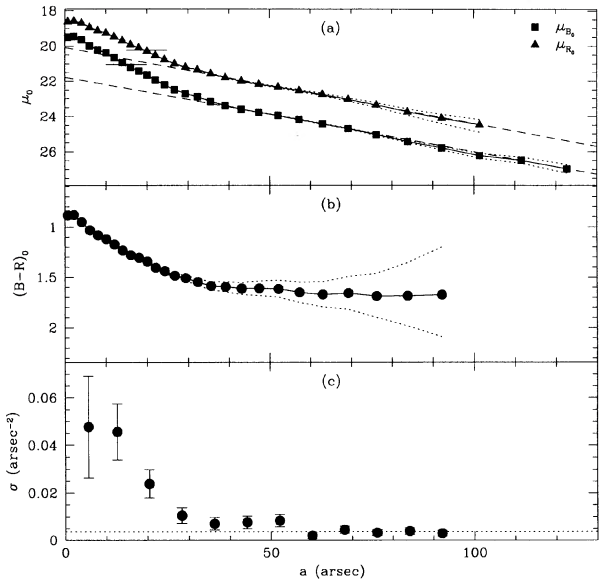

FIG. 5. Azimuthally averaged radial profiles of various quantities. (a) Shows the extinction corrected surface brightness profiles in B and R. The dotted lines show the effect of changing the sky level by $\pm 1\sigma_{sky}$. The dashed lines show the exponential profile fits using the points with $a>35''$. The short horizontal bars indicate the sky level in each band. (b) Shows the reddening corrected color profile. The dotted lines indicate the effect of varying the sky level simultaneously by $1\sigma_{sky}$ in each band. (c) Shows the radial surface density of embedded objects with $18 \leq m_R < 25$ and $B-R<2.5$. Errors are from $n^{1/2}$ statistics. The dotted line shows the background density.

The galactic and LMC extinction laws of Howarth (1983) were adopted for removing respectively $E(B-V)_f$ and the remaining portion of $E(B-V)_{em}$. The adopted values for $E(B-V)_f$ and $E(B-V)_{em}$ are listed in Table 1. Only emission line relative fluxes are dereddened by $E(B-V)_{em}$; the continuum reddening is lower (Sec. *4.3*). The fluxes are relative to Hβ which has an observed intensity of $I_{H\beta}=4.5\times10^{-13}$ erg cm^{-2} s^{-1} over the $4''\times72''$ extraction aperture of the slit.

The region from Hβ to [O III]5007 Å was fitted with multiple Gaussians because of the presence of strong Hβ absorption and so as to use the fit as a template in measuring radial

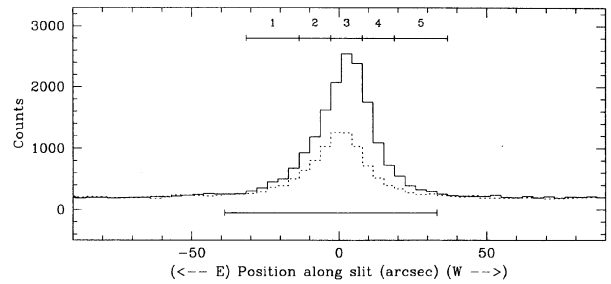

FIG. 6. Distribution of [O III] 5007 Å (solid line) and continuum light (dotted line) along the spectrograph slit. The long bar below the plot indicates the aperture size used to extract the large aperture spectrum. The numbered short bars indicate the apertures used to extract the spectra for measuring the velocity gradient along the slit.

velocity shifts along the slit. Four components were used; three for the emission lines (Hβ, [O III]4959,5007 Å) and one for the Hβ absorption. The components were constrained to have the same velocity, and the emission lines' widths were set to the instrumental resolution (none of the emission lines are significantly broadened). A smooth continuum was fitted by eye. The spectrum in this region and its fit are illustrated in Fig. 8(a). The resultant Hβ absorption equivalent width is 9.6 Å. Figures 8(b)–8(f) show the spectra extracted with the small apertures. Velocity shifts were measured by cross correlation, using this fit (but with a flat continuum) as the template. This template was also employed on spectra extracted from the individual exposures of NGC 2915. For comparison, relative shifts in two arc spectra extracted using the same apertures were measured with an appropriate template.

Figure 9 shows the results for the summed and constituent spectra. There is a velocity gradient of 61 km s^{-1} from aperture 1 to 5. The velocity structure along the slit for the sum spectra is mirrored in detailed in the constituent spectra. The measurements were repeated using just the [O III] lines in the template. This yields the same gradient between apertures 1 and 5. The arc spectra results do not show this gradient. Their dispersion about the mean in V_r is 5.5 km s^{-1}, with, at most, a 17 km s^{-1} velocity gradient between apertures 1 and 5.

4. PROPERTIES OF NGC 2915

4.1 Morphology and Stellar Populations

Figure 5 shows that there is a fundamental difference in the contents of NGC 2915 between the core region and the rest of the galaxy. Beyond $a\approx35''$ the surface brightness distribution is smooth and exponential and has a nearly constant color. Interior to this radius the surface brightness increases quicker than the exponential fit to the outer portions, and the colors become bluer. The galaxy becomes more lumpy with the density of embedded objects increasing markedly. As well, all of the ionized gas in the images of SD and Marlowe *et al.* (1994) is located within this radius. Thus, there are two stellar populations in NGC 2915 a red diffuse population with an exponential light distribution, and a bluer core population.

The core population is the locus of current high mass star formation (hence the H II). The Hβ absorption equivalent width (9.6 Å; which is only determined in the core) is a further indication of the presence of a young stellar population there, since equivalent widths are not larger than ~3 Å in old stellar populations like those in globular clusters and elliptical galaxies (Burstein *et al.*, 1984).

Note that it is the core population that defines NGC 2915's BCD nature. MFDC make the same point concerning NGC 1705. If only the diffuse population is considered, NGC 2915 looks more like a dE galaxy. Its color $(B-R)_0 = 1.65$ is typical of old stellar populations as in normal ellipticals (Peletier *et al.*, 1990), and is redder than the outlying colors in either M32 ($B-R=1.40$) or NGC 205 ($B-R=1.25$) (Peletier, 1993). Therefore it is either fairly old, or has a low rate of high mass star formation. Although

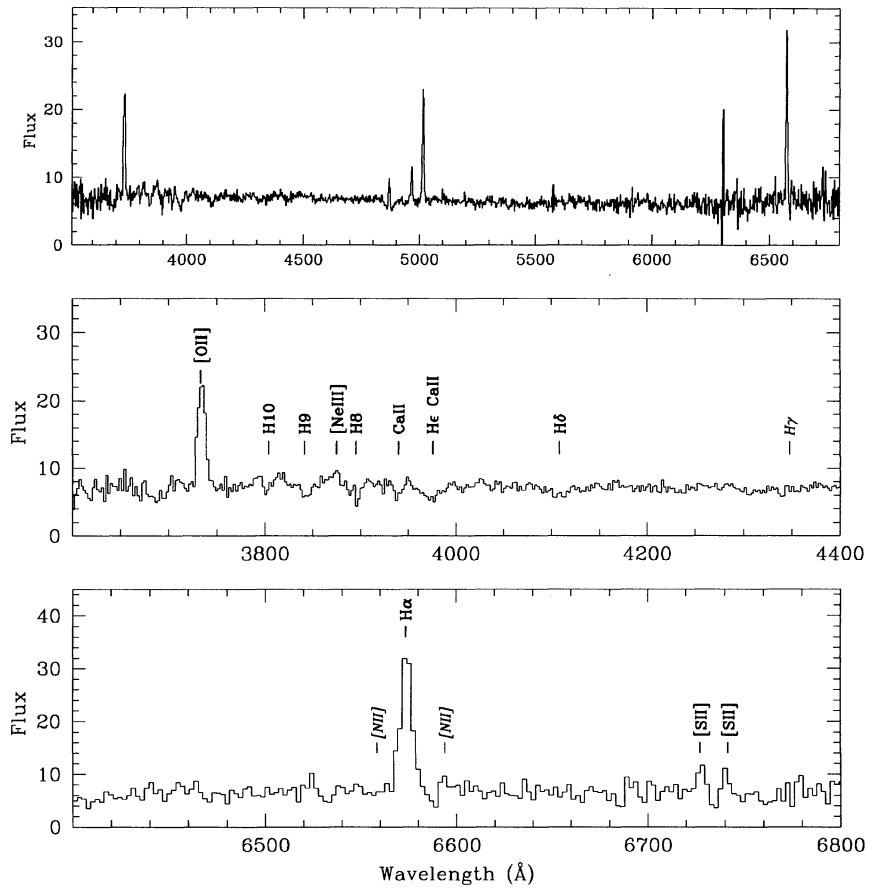

FIG. 7. Large aperture spectrum of NGC 2915. Flux units are 10^{-14} erg cm^{-2} s^{-1}. Top panel shows the full flux calibrated spectrum. Lower two panels expand the red and blue portions of the spectrum and show line detections (bold font) and where nondetected lines should fall (italics, smaller font).

the surface brightness profile resembles those of other BCDs, it is also akin to a subset of dE galaxies (the type IIIa profiles of Binggeli & Cameron 1991). The value for $B(0)_c$ (presumably what the central surface brightness would be in the absence of a core population) is like that of low surface brightness dwarfs. Thus NGC 2915 is a BCD with some properties like dE galaxies, especially at large radii.

TABLE 6. Emission line data.

i.d.	$100(I/I_{H\beta})$	$100(I/I_{H\beta})_0$
[O II] 3727	342 ± 16	542 ± 26
[Ne III] 3869	21 ± 11	32 ± 16
Hβ	100 ± 6	100 ± 6
[O III] 4959	99 ± 6	96 ± 6
[O III] 5007	314 ± 7	299 ± 7
Hα	437 ± 24	286 ± 16
[N II] 6584	< 22	< 13
[S II] 6716+6731	70 ± 32	44 ± 20

4.2 Nature of the Embedded Objects

The embedded objects are associated with the core population. Figure 5(c) shows the surface density of sources with $18 \leq m_R < 25$ and $(B-R) < 2.5$. The density of embedded objects falls to the foreground level, $\sigma = 3.8 \pm 0.4 \times 10^{-3}$ arcsec^{-2} (determined from the sources with $a > 106''$) by $a \approx 60''$. This discussion will concentrate on the objects with $R < 30''$ which are listed in Table 3, and identified in Fig. 3. Of these 52 objects ~11 are expected to be in the foreground (we do not attempt to determine which). The remaining objects form a more flattened system than the neighboring isophotes, having $a/b \approx 2.6$,[6] compared with an average $\overline{a/b} = 1.8$ for the isophotes with $a < 35''$. This flattening is readily apparent in Fig. 2(d). There is no significant difference in the position angle of the embedded object distribution ($\phi = -48^{\circ}2$), compared to that of the isophotes.

[6]Found by applying the moment analysis technique discussed above to the central sources after correcting the moments for the expected contribution of 11 uniformly distributed foreground sources.

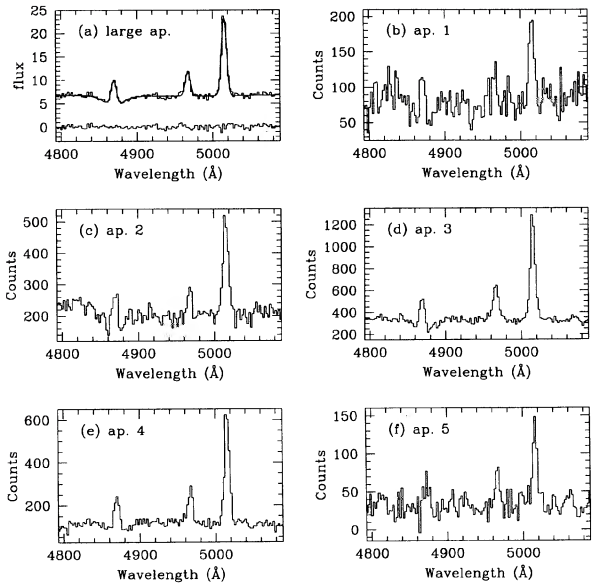

FIG. 8. Spectrum of the region centered on Hβ and [O III]4959,5007 Å. Panel (a) shows the flux calibrated spectrum extracted with the large aperture (upper histogram style line), the fit to the data (smooth line) and the residuals of the fit (lower histogram style line). Flux units are 10^{-14} erg cm^{-2} s^{-1}. Panels (b) through (f) show the spectra (not flux calibrated) extracted through the small apertures.

At 20″ from the center, objects with a magnitude of 20.8 in either band have the same flux as the underlying surface brightness integrated over the seeing disk. The faintest objects have an intensity that is a small fraction of this. Their low intensities are in the regime of the surface brightness fluctuations (Tonry & Schneider 1988) expected when a galaxy is just beyond the limits of resolution. In such cases

$$\frac{I_F}{2\pi r^2 S} \approx \frac{1}{\sqrt{n}} < 1,$$

where I_F is the fluctuation intensity (about the intensity of the brightest stars), S is the surface brightness, r is the seeing radius, and n is the number of stars with intensity $\sim I_F$ within the seeing disk. Although we have not measured the fluctuation intensity, it is likely that it is equivalent to, or perhaps slightly fainter than the faintest objects detected here. In this case the objects causing the fluctuations are supergiant stars instead of giants as is the case of galaxies usually examined for surface brightness fluctuations.

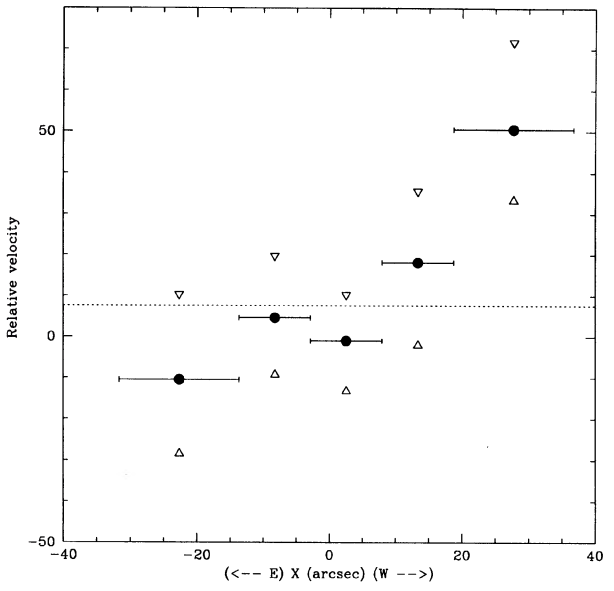

FIG. 9. Relative velocity measurements along the slit. The velocities are relative to the template. The ● symbol corresponds to the combined spectrum, while ▽ and △ correspond to, respectively, the first and second of the constituent exposures. The x axis errorbars shows the aperture size. The dotted line at ΔV_r=7.6 km s^{-1} shows the adopted central velocity.

This identification follows from the color magnitude (c–m) diagram shown in Fig. 10. For comparison the c–m diagram for the objects in NGC 5253 (CP) is also shown. Evolutionary tracks of massive stars are overlayed on both panels. Like in NGC 2915, the objects in NGC 5253 are part of its blue core population. Sandage *et al.* (1994) show that most of these are individual massive stars. Likewise, most of the embedded objects in NGC 2915 are also either individual stars or blends of a few such stars. Since many have brightnesses clearly exceeding the underlying surface brightness, NGC 2915 is starting to be resolved. The large number of blends, as indicated by the number of flagged objects in Table 3, shows that it is not fully resolved. Figure 10 suggests we are seeing stars up to $\sim 25 \mathcal{M}_\odot$ in the cores of these two galaxies. This is not surprising since the relatively blue core colors and presence of H II indicates that high mass star formation is expected there.

The five brightest objects in NGC 2915 and NGC 5253 are probably young star clusters or associations. In NGC 2915, these are objects 1, 2, 3, 4, and 110 which have $\overline{B-R} = 0.66$. In the case of NGC 5253 the five brightest objects are too luminous to be single stars. For those in NGC 2915, although their luminosity and colors can be modeled by single stars with initial masses $25 < \mathcal{M}/\mathcal{M}_\odot < 60$, their extended appearance indicates that they are not single stars. In both galaxies these objects form a clump in the c–m diagram, with a mean color close to that expected for young clusters with little internal extinction. This is illustrated in Fig. 10 by showing a vertical mark at the mean color [$(B-V)_0$=0.19, $(B-R)_0$=0.40 after correcting for only the foreground component of extinction] of the RH, Y2, and Y3 groups of Bica *et al.* (1990). These are their spectral groups for clusters with ages $\lesssim$100 Myr, excluding their Y1 group, which corresponds to the brief red-supergiant phase. Objects 2, 3, and 4 are Hα bright and in the cores of the two brightest H II regions (seen in the Marlowe *et al.* 1994 images), which suggests that they are the ionizing clusters. Similarly, in NGC 5253 the five brightest objects are contained in a small region where the emission lines are most intense (cf. CP with Walsh & Roy 1989).

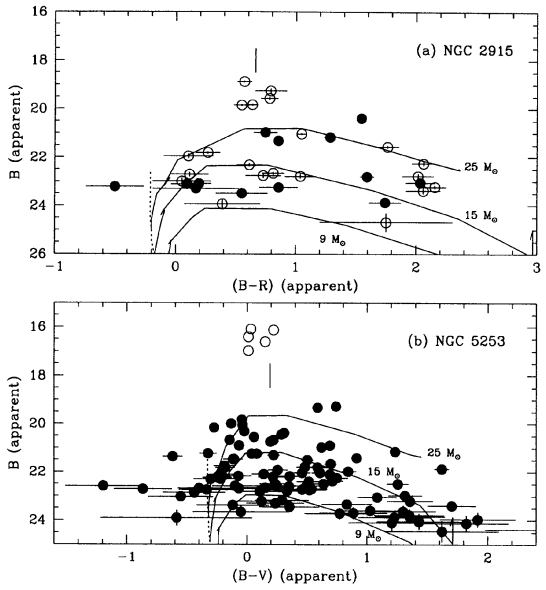

FIG. 10. Color–Magnitude diagrams of embedded objects in (a) NGC 2915, and (b) NGC 5253 (using the data of CP). Apparent magnitudes and colors (note different colors) are plotted. Open symbols indicate the flagged entries in Table 3 in panel (a), and the central objects of NGC 5253 in panel (b). The main-sequence (dotted line) and evolutionary tracks (solid lines) of 25, 15, and 9 $\mathcal{M}_\odot$ stars are shown after correcting for the distance and reddening. The reddening vector for NGC 2915 is shown in the upper left of panel (a). The reddening of NGC 5253 is $E(B-V)=0.0$ (Sandage *et al.* 1994). The vertical mark at $m_B=18$ shows the expected color of young clusters (following Bica *et al.* 1990) after correcting for just foreground (galactic) reddening. The main-sequence and evolutionary tracks are from Maeder & Meynet (1988) converted to the observational plane using the method of Doyon *et al.* (1994; Appendix B) with conversion to $(B-R)$ following Johnson (1966) and Bessell (1979).

4.3 Reddening and Distance

$E(B-V)$, is derived by comparing the observed and expected colors (see above) of the cluster candidates. This yields a total reddening $E(B-R)=0.26\pm0.07$, which corresponds to $E(B-V)=0.15\pm0.04$. This is the adopted reddening for the broadband and continuum light. The difference between this and Burstein & Heiles (1984), value for $E(B-V)_f$ is negligible relative to the uncertainties. The reddening derived from the Balmer decrement is a bit higher $E(B-V)_{em}=0.41\pm0.15$. This was determined from the Hα/Hβ decrement and the standard assumptions (e.g., Salzer *et al.* 1989): that the intrinsic Balmer decrement is due to case B recombination in an optically thin plasma with $T_e=10^4$ K as calculated by Osterbrock (1989). The error is mainly due to the adopted relative flux uncertainty of 10%. Although this discrepancy is only a 1.7σ detection, it is in the usual sense that a higher value is found from the Balmer decrement than when other reddening indicators are used (e.g., MFDC; Fanelli *et al.* 1988). The geometry of the system is the usual explanation for such discrepancies; e.g., the continuum is seen through holes in the dust distribution which is correlated with the ionized gas distribution. NGC 2915 isn't very dusty like other dAgs such as NGC 3077 (Price & Gullixson 1989), but does appear to have some faint dust clouds with offset positions 10″E, 16″S (elongated along major axis, and bordering objects 110, 116, 118); 0.5″W, 10″N; and 6″W, 10″N. Because of the large uncertainty in $E(B-V)_{em}$, it is only used to deredden the emission line relative fluxes.

D is derived relative to NGC 5253 by comparing the objects that are most likely to be stars. The absolute B magnitude of the brightest objects in each galaxy is assumed to be equal, after excluding the cluster candidates. The object that meets these criteria in NGC 5253 is 22 with $m_b=19.27$ from CP, and for NGC 2915 its object 101 with $m_b=20.39$. After correcting for extinction this yields $D_{\rm NGC\ 2915}/D_{\rm NGC\ 5253}=1.3\pm0.4$. The uncertainty is derived from the errors in A_B and the magnitude separation between the brightest and second brightest object meeting the above criteria. Scaling to the distance of NGC 5253 leads to our adopted $D=5.3\pm1.3$ Mpc for NGC 2915. The underlying assumption of this method is that these galaxies have similar IMFs, metallicities, and crowdings in their core populations. If so, the objects will display similar upper envelopes in $c-m$ diagrams. This is the best distance estimate possible with the present data, but it should still be considered tentative. A way of improving the distance estimate to nearby BCDs is discussed in Sec. 6.

4.4 Aligned Structures?

It is peculiar that many of the objects in NGC 2915 appear to be connected or aligned. This is most noticeable on the SE side of the galaxy where there appear to be three parallel lines of objects each about 11″ long and separated by 4″. Their orientation is nearly parallel to the major axis and they stretch between (1) object 118 and 110, (2) 117 to 111, and (3) 115 to 104. This is also the direction of elongation of some sources, including the components of object 110 and several faint "wisps" (thin linear features). These are identified in Fig. 2(c). Some of these wisps appear to be attached at one end to embedded objects (111, the two components of 103) giving them a cometary or tadpole appearance. In all cases the tails point away from the center of NGC 2915. Further out, another linear feature extends out to 61″ and connects some faint embedded objects to form the SE ejecta noted by SBC. This is best seen in Fig. 2(d) which is a version of the B band lumpy image that enhances features with scale sizes up to 6″.

The line of objects from 110 to 118 coincides with the jet seen by SBC and SD in their Hα+continuum photograph. However, the continuum and Hα images of Marlowe *et al.* (1994) clearly show that it is a continuum feature. In their images there are two prominent but low surface brightness Hα bubbles, one to the NE, the other to the SE of NGC 2915's center, each having a diameter of ~30″. The "jet" is clearly in the central hole of the SE bubble. This suggests the features on the SE side of the galaxy are related to the expansion of this bubble. On the NW side we can see the other ejecta of SBC (extending out to 45″), which takes the form of a curved strand connecting a few embedded objects giving the appearance of a thin spiral arm. Since there are no other such structures on this side, and it does not appear to be

associated with any Hα structures, it is more likely to be due to the chance alignment of unrelated objects.

4.5 Dynamics

Detailed discussions of NGC 2915's dynamics will be deferred to Paper II. Preliminary H I results from that study confirm the presence of a gradient in the same sense seen in the optical spectra; the east side is approaching and the west side is receding. They also indicate that the H I dynamics are dominated by circular rotation (in a plane near that expected from the optical orientation), but that there are some regions of noncircular motion especially at the center of the SE bubble. Although the spectrum's slit does not fall on either Hα bubble, it passes near them. Thus the velocity gradient may be in part due to expansion. Nevertheless, we will assume, for the moment, that the gradient is due to rotation alone.

To transform the gradient into a rotation velocity, the average V_r of the inner three apertures is used to define the central velocity, and the outer two apertures are used to define the magnitude of the gradient. This yields a gradient of $\Delta V_r = 30 \pm 13$ km s^{-1} at a distance $\Delta x = \pm 25''$ from the slit center. For an inclination $i = 52°$ [from the local a/b and assuming an intrinsic flattening $c/a = 0.22$; Bottinelli *et al.* (1983)], this projects to a rotation velocity $V_R = 50 \pm 21$ km s^{-1} at $a = 32''$. The corresponding dynamic time scale is $\tau_{\rm dyn} = (G\rho)^{-1/2} = 33$ Myr. The interior mass and mass-to-light ratio is $\mathcal{M} = 4.8 \times 10^8 \mathcal{M}_\odot$, and $\mathcal{M}/L_B = 1.3 \mathcal{M}_\odot / L_{B,\odot}$. If noncircular motions contribute to the gradient, then $\tau_{\rm dyn}$ will be underestimated and $\mathcal{M}$ and $\mathcal{M}/L_B$ will be overestimated. Regardless, it is clear that the local dark matter content is not very high for the optical core of NGC 2915. This does not apply globally since the dark matter distribution in galaxies is invariably more diffuse than the luminosity distribution.

The rotation seen in NGC 2915 may explain the high flattening of the embedded object distribution. That is, these objects are equivalent to extreme Population I objects in disk galaxies, which form in a disk even flatter than other Population I objects.

5. ANATOMY AND EVOLUTION OF NEARBY BCDs

5.1 Comparison with other BCDs

The three dAg/BCDs noted in Sec. 1 are near enough to resolve individual stars, thus allowing one a detailed look at their anatomy. Therefore we concentrate on these objects, using here the following sources. NGC 1705: MFDC; NGC 2915; this work, SBC, SD, Marlowe *et al.* (1994); NGC 5253: CP, SD, Bottinelli *et al.* 1990, Walsh & Roy (1989), Sandage *et al.* (1994). Table 7 compares some salient properties of these galaxies. Our adopted distance, D, and reddening, E$(B-V)$, yield the absolute magnitude M_{B_T}. The distance to NGC 1705 has been adjusted from that in MFDC to correspond to $H_0 = 50$ km s^{-1} Mpc^{-1} in order to be compatible with the relatively long distance scale adopted for the other two galaxies. Table 7 lists $M_g = 4/3 \mathcal{M}_{\rm H\,I}$, the neutral gas mass; $d_{\rm core}$, the core population diameter; $L_{\rm H\alpha}$, the Hα luminosity; and SFR, the star formation rate estimated from $L_{\rm H\alpha}$ following Kennicutt [(1983); who uses an "extended"

TABLE 7. Properties of dAg/BCDs.

Quantity	NGC1705	NGC2915	NGC5253	units
D	7.1	5.3	4.1	Mpc
$E(B-V)$	0.05	0.15	0.00	mag
$M_{B_{T,0}}$	−16.55	−15.90	−16.95	mag
M_g	2.6	9.1	5.9	$10^8\ M_\odot$
$d_{\rm core}$	1.4	1.8	2.8	Kpc
α_B^{-1}	0.52	0.66	0.56	Kpc
$L_{\rm H\alpha}$	1.5	0.6	6.5	10^{40} erg
SFR	0.13	0.05	0.58	$M_\odot$ yr^{-1}
$L_{B,cl}$	127	2.3	6.4	$10^6\ L_{B,\odot}$
τ_{cl}	13	≤ 30?	≤ 30	Myr
M_{cl}	34	$\lesssim 1$	$\lesssim 4$	$10^5\ M_\odot$
$\tau_{\rm cross}$	27	35	54	Myr
$\tau_{\rm dep}$	2.0	18	1.0	Gyr
τ_*	2.5	3.6	0.6	Gyr

Miller–Scalo IMF with mass limits of 0.1 and 100 $\mathcal{M}_\odot$). We also list properties of the brightest star cluster in each galaxy namely $L_{B,\rm cl}$, its luminosity; $\tau_{\rm cl}$, its estimated age (limit); and $\mathcal{M}_{\rm cl}$ an estimate of its mass [the mass-to-light ratio used was derived from the age and the models of Struck-Marcell & Tinsley (1978)]. The age of NGC 1705's cluster is derived in MFDC. The age limit of NGC 5253's cluster is derived from the $(U-B)$, $(B-V)$ colors of the five brightest clusters in this galaxy using the same method as MFDC. Only one color is available for NGC 2915's clusters, so a good estimate of $\tau_{\rm cl}$ is not possible. We assume that the same limit on $\tau_{\rm cl}$ for NGC 5253 applies here as well. Finally, three more time scales are also listed in Table 7: $\tau_{\rm cross}$ is the crossing time for a particle traveling at 50 km s^{-1} (meant to represent typical gas velocities in NGC 2915) to traverse $d_{\rm core}$; $\tau_{\rm dep} = M_g/{\rm SFR}$ is the gas depletion time scale; and $\tau_* = L_B(\mathcal{M}/L_B)/{\rm SFR}$ is the time to build the stellar content of the galaxies at the present SFR. Here we assume $\mathcal{M}/L_B = 0.5$ which seems to be appropriate for the stellar content of NGC 1705.

The most important similarity between these galaxies is that each is composed of two distinct stellar populations; a relatively blue core and redder diffuse population. The core population is a few Kpc across in each case. Although the isophote centers wander with radius it is clear that the core population has a fairly central location in these galaxies, since the outer isophotes' centers are firmly within the population area. Therefore we classify them as nE type BCDs in the subclassification scheme of Loose & Thuan (1985); that is they have a single central nuclear star-forming complex, and smooth elliptical outer isophotes. The core population defines this nuclear complex, while the outer isophotes mark the diffuse population. In each case individual massive stars, intense H II emission, and young star clusters can be dis-

cerned in the core, where they are largely confined. This indicates that the core population is the site of current high-mass star formation.

The core population is also good at manufacturing star clusters. The maximum cluster luminosity, $L_{B,\mathrm{cl}}$, varies greatly from galaxy to galaxy. In NGC 2915 $L_{B,\mathrm{cl}}$ is three times fainter than for NGC 5253, and nearly 60 times fainter than the central cluster of NGC 1705. The mass, M_{cl}, of this cluster should only be considered indicative because of the uncertainty of estimating ages and $\mathscr{M}/L_B$ ratios. Nevertheless it is clear that $\mathscr{M}_{\mathrm{cl}}$ varies by at least a factor of 30 between galaxies, with clusters as massive as the most massive galactic globular clusters seen. Note that here only the brightest, and usually youngest, clusters of each galaxy are considered. MFDC note that even the most massive globular clusters would look pretty inconspicuous in these types of galaxies if they are older than a few Gyr.

The galaxies differ in color and spectral properties of their populations. In their cores, NGC 5253 has the bluest and highest excitation spectrum, while NGC 2915's is the reddest. The diffuse population of NGC 1705 [$(B-V)_0=0.44$, $(B-R)_0=0.99$] is bluer than either NGC 5253 [$(B-V)_0=0.55$] or NGC 2915 [$(B-R)_0=1.65$]. These differences show that the detailed star-formation and/or enrichment histories of these galaxies are different, despite their morphological similarities. It is a bit tantalizing (but probably merely fortuitous) that the exponential scale length of the diffuse population is 0.6 Kpc for all three galaxies. The dAg/BCDs do not share the same environment. NGC 5253 is in the Cen A group, while NGC 1705 and NGC 2915 are relatively isolated. All three dAg/BCDs have faint bubbly and filamentary Hα structures. This is most spectacular for NGC 1705 which appears to be undergoing a galactic wind.

It is interesting that the SFR ranges from low (NGC 2915 and NGC 1705) to moderate (NGC 5253) in these galaxies. The corresponding τ_* and τ_{dep} is on Gyr time scales. These provide rough fuel consumption limits to star-formation duration in the past and future at the present SFR. The BCDs in the sample of Sage *et al.* (1992) have somewhat higher SFRs (on average) and their values of τ_{dep} range from 0.07 to 1.7 Gyr. Sage *et al.* note that these values are like those found in normal spirals, and therefore that BCDs are only as efficient as spirals in forming stars.

Although the morphology of the dAg/BCDs are similar to each other, and some other BCDs, it should be remembered that the BCD classification is not homogeneous (Loose & Thuan 1985; Kunth *et al.* 1988). For example, the dAg/BCDs do not resemble the very compact BCDs studied by Drinkwater & Hardy (1991). Six of the eight galaxies in that sample are exponential from their center out to the 26 mag arcsec^{-2} isophote; only one (RMB 56) has an exponential plus core structure. It appears that these galaxies have only one stellar population, and thus may represent BCDs without an older outlying population. However, the seeing in their observations is comparable to the scale size of the galaxies, so higher resolution observations are required to confirm this result.

5.2 Starbursts and the Evolution of BCDs

Some important question about BCDs are: how are they related to other types of galaxies? and how do they evolve? The morphological similarities between BCDs and dE galaxies have been noted by Bothun *et al.* (1986), amongst others. For the dAg/BCDs this similarity is most noticeable outside the core where the diffuse population dominates and the isophotes are smooth and elliptical. Transition cases between the two types may exist. For example, except for its lack of bright emission lines, NGC 205 could be classified as a BCD. These similarities suggest an evolutionary link between BCDs and dEs. However, it is not clear which way the link goes. For example, CP argue that NGC 5253 was originally a dE whose current star formation may be fueled by accretion from another galaxy in the Cen A group, while MFDC argue that NGC 1705 is a BCD in the process of shedding its ISM in a galactic wind to become a dE.

The observations of NGC 2915 further complicate the picture. H I observations indicate that the neutral component of its ISM is massive and in stable circular rotation (Becker *et al.* 1988; Paper II) and thus unlikely to be totally disrupted by the central star formation. Similarly it is hard to imagine it accreting such a large amount of H I in its relatively isolated environment, although tidal interaction with SGC 0938.1−7623, should it prove to be a companion, might be responsible for its central star formation. Thus NGC 2915 looks like a BCD in a relatively stable configuration.

The mechanism most commonly invoked to characterize BCD evolution is the starburst—a short duration ($\lesssim$10 Myr typically quoted) event of increased star-formation greatly above the average rate. Indications for starbursts occurring in BCDs come from population modeling of their spectra (Fanelli *et al.* 1988; Mas-Hesse & Kunth, 1991; Cerviño & Mas-Hesse, 1994). Bursts are particularly appealing for BCDs with Wolf-Rayet features in their spectra, since their strengths can not be modeled with continuous star-formation models, but require bursts with ages (and hence durations) $\lesssim$5 Myr (Cerviño & Mas-Hesse 1994; Vacca & Conti 1992).

Despite this evidence, there are good reasons to doubt that even the core populations of the dAg/BCDs, which defines their BCD nature, result from such short duration bursts. Recall that the original theoretical reason for invoking starbursts was to satisfy closed box chemical evolution models (e.g., Searle & Sargent 1972; Thuan 1987); without bursts, too many metals would be produced over the BCDs lifetime. However, the existence of winds (e.g., in NGC 1705) invalidates closed box chemical evolution models for BCDs, especially since during a wind, the hot metal-enriched ISM preferentially escapes (Vader 1986; De Young & Gallagher 1990). Other limits to star-formation duration are not so strong. Loose upper limits are placed by τ_{dep} and τ_*, which (as noted in Sec. *5.1*) yield values up to a few Gyr for BCDs. A lower limit is given by τ_{cross} since the coherent formation of a stellar population requires information to be passed from one side of the population to the other. Thus applying basic considerations only limits star formation duration from a few tens of Myr to a few Gyr for the dAg/BCDs.

There is indeed some evidence for extended duration

(>10 Myr) star formation in the cores of the dAg/BCDs. Individual supergiants, both red and blue, can be seen at similar magnitudes in all three dAg/BCDs [but most convincing in *Hubble Space Telescope* images of Sandage *et al.* (1994)]. Both types of stars should not be present in an instantaneous burst (Cerviño & Mas-Hesse 1994). Both NGC 2915 and NGC 1705 contain variety of objects $\lesssim$10 Myr old (individual stars, H II regions, clusters) but have integrated core colors suggesting an older post-burst population; the central colors of NGC 2915 [$(U-B)_0=-0.30$, $(B-R)_0=0.78$, for aperture diameters $\lesssim$33.8″ in Table 2] can be modeled by a 100 Myr old burst comprising only 1% of the stellar mass (Krüger *et al.* 1991), while MFDC derive an age of 50 Myr for NGC 1705's core if it was produced in a burst. Although it may be possible to produce colors like those seen in the cores of NGC 1705 and NGC 2915 during the brief red-supergiant phase of an instantaneous burst (at $\tau\approx$10 Myr; Cerviño & Mas-Hesse 1994; Heckman & Leitherer 1993) this phase will be washed out in their cores by the minimum star-formation duration set by $\tau_{\rm cross}$. This combined presence of objects a few Myr old and integrated colors indicative of an older population suggest some form of continuous star formation.

So how does one reconcile the evidence for bursts <10 Myr old seen in some BCD spectra, with the above arguments for a more extended duration of star formation? In some cases it may be due to the nonhomogeneity of the BCD class. The previous paragraph mainly applies to the dAg/BCDs which are relatively large and have a regular morphology. The smallest BCDs, such as I Zw 18, have star-forming regions only ~100 pc across. A shock traveling at 50 km s^{-1} can traverse that distance in 2 Myr allowing relatively rapid and coherent changes in the star-formation rate in such a region. Other BCDs, such as II Zw 40, have peculiar morphologies suggesting strong interaction (Baldwin *et al.* 1982; Brinks & Klein 1988) which may be triggering a starburst.

Alternatively, if a dwarf galaxy is observed during or just after the formation of a massive star cluster one would derive a high SFR, low $\tau_{\rm dep}$, and may see Wolf-Rayet features in the spectrum if the observer centers the slit on the brightest object: the young cluster (and if observed during the Wolf-Rayet phase). This is exactly what is happening in NGC 5253 which has the highest SFR, and lowest $\tau_{\rm dep}$ of the dAg/BCDs. It has Wolf-Rayet features in its spectrum, but only at the position of its brightest cluster (Walsh & Roy 1989). A more spectacular example would have been NGC 1705 in the first 2–3 Myr after the formation of its central cluster. Then its Hβ luminosity would have been $L_{\rm H\beta}\approx5\times10^{40}$ erg s^{-1} [from the models of Mas-Hesse & Kunth (1991), and the IMF used by MFDC, which has mass limits of 0.1 and 120$\mathcal{M}_\odot$) if the nucleus was the sole ionizing source, and we would have derived SFR$\approx$1.4$\mathcal{M}_\odot$ yr^{-1} and $\tau_{\rm dep}\approx$0.2 Gyr. Compared to Salzer's *et al.* (1989) survey of emission line galaxies (after correcting for their value of H_0) NGC 1705 would have been in the top 25% of galaxies with $M_B>-18$ in terms of $L_{\rm H\beta}$; currently it is at the bottom 30%.

Thus, the starburst model is probably appropriate for even relatively large BCDs with regular morphologies. However, the starburst should not be identified with either the galaxy as a whole, or the core population as a whole, but with individual massive ($\gtrsim10^6\mathcal{M}_\odot$) star clusters in the core population. Thus a starburst would cover only a small fraction of the parent galaxy and can be very rapid ($\ll$1 Myr; Larson 1988). For the first few Myr of such a cluster's life the galaxy would have characteristics of more extreme BCDs such as Haro 2 (Sage *et al.* 1992). The properties become less extreme as the ionizing flux from the cluster rapidly declines. Between bursts there is sufficient high mass star formation throughout the core (in the form of individual stars and less massive clusters and associations) for the galaxy to retain its BCD morphology, but with less extreme characteristics, such as those of NGC 2915. To put it succinctly, we propose that the burst phase of a BCD corresponds to the formation of a massive cluster, and the interburst phase is still a BCD but with less extreme characteristics.

The manufacture of a massive cluster results in a galactic wind which is powered by stellar winds and supernovae from its high mass stars. This serves to release the metals synthesized by the high mass stars and perhaps expel a significant fraction of the ISM. As the ISM is depleted by winds and locked up into stars, the morphology becomes more and more like a dE or nucleated dE (with the nucleus being the most massive cluster formed). In the absence of external influences, the evolution to a dE morphology would then occur on ~Gyr (gas depletion) time scales.

6. CONCLUSIONS

NGC 2915 is a BCD galaxy, although at large radii it has some properties similar to dE galaxies; namely smooth elliptical isophotes, a red color [$(B-R)_0=1.65$], and a low extrapolated central surface brightness [$B(0)_c=22.44$ mag arcsec^{-2}]. It has two stellar populations; a red diffuse population with an exponential surface brightness distribution, and a bluer high surface brightness core. The high excitation emission line spectrum in the core indicates a maximum metallicity of about half solar. The Balmer series is seen in absorption as is Ca II, although the latter probably is contaminated by galactic interstellar absorption. The core population is the locus of current high mass star formation. It is contained in a diameter of 70″=1.8 Kpc, where the surface brightness exceeds the exponential fit to the outer portions. Numerous embedded objects are concentrated in this area as is the ionized gas.

The brightest embedded objects are young ionizing clusters or associations with masses up to ~$10^5\mathcal{M}_\odot$. They have little reddening after correcting for galactic extinction. The colors and magnitudes of the remaining objects are consistent with supergiant stars with initial masses up to ~25$\mathcal{M}_\odot$. The distance relative to NGC 5253 is 1.3±0.4 (an absolute distance $D=5.3\pm1.6$ Mpc), derived by assuming that the brightest embedded object (excluding likely clusters) in each galaxy has the same B magnitude.

The embedded objects form a more flattened system than the underlying isophotes, suggesting they are in a disk like structure. There are numerous curious structures on the SE side of the galaxy. These include the "ejecta" of SBC and SD, rows of apparently aligned objects, faint thin wisps, and

an elongated dust cloud. These are all oriented nearly parallel to the galaxy's major axis. Some of the wisps appear to be connected at one end to embedded sources, giving them a cometary or tadpole appearance. The tails of these objects all point away from the center of NGC 2915. Another of SBC's ejecta is seen in the NW side. It is dotted with embedded objects, and forms a curved structure resembling a thin spiral arm.

There is a significant velocity gradient in the spectra. Although noncircular motions may contribute somewhat to this gradient, rotation probably dominates. If so, the projected rotational velocity is $V_R = 50 \pm 21$ km s^{-1} at the isophote with $a = 32''$. The interior $\mathcal{M}/L_B \approx 1.3 \mathcal{M}_\odot/L_{B,\odot}$ is not high for dwarf galaxies, but only indicative of the optical core of the galaxy.

There are at least three dAgs that can be classified as a BCD (NGC 1705, NGC 2915, and NGC 5253). All three have similar population distributions and contents. All would be classified as nE type BCDs in the scheme of Loose & Thuan (1985).

The presence of winds in BCDs invalidates closed box chemical evolution models and means that observations no longer limit overall star formation to occur in short duration (<10 Myr) bursts. A plausible scenario for the evolution of the dAg/BCDs involves continuous formation of high mass stars in the core population over Gyr time scales. Star clusters also form in the core; each forming in <1 Myr and thus representing mini-bursts of star formation. If spectroscopic observations are preferentially centered on such clusters, the results would be biased towards indicating the dominance of short duration starbursts. It is important to note that there are few hard constraints on the formation time scale of BCD cores. Anything between a few tens of Myrs to a few Gyr are possible (for the dAg/BCDs). The reason for positing the above scenario is to illustrate that BCD evolution need not be as rapid as commonly envisioned. Instead the BCD morphology may be relatively stable, with slow evolution into a dE morphology occurring on ~Gyr time scales.

Higher quality data, currently obtainable with modern instrumentation, would improve much of our knowledge of NGC 2915 and other nearby BCDs. There are at least three dAg/BCDs near enough to resolve stars with $\mathcal{M} \gtrsim 9 \mathcal{M}_\odot$, and thus probe the star formation history over a few tens of Myr. It may be possible to probe for fainter stars in their low surface brightness populations by examining surface brightness fluctuations (Tonry & Schneider, 1988) or pixel intensity distributions. High resolution ($\ll 1''$) imaging would increase the contrast of the brightest stars with the underlying high surface brightness background, allowing distances to BCDs to be measured directly from analysis of their Cepheid variables (e.g., Sandage *et al.* 1994) or long period variables (Pierce & Crabtree 1993).

We thank Despina Hatzidimitriou for assisting in the AAT observations, and Barry Croke for forwarding archival results of AAT standard star observations. Jean-François Bertrand kindly explained how to use the IRAF program NGAUSFIT. This paper benefited from useful discussions with M. Bessell, R. Doyon, H. Ferguson, T. Heckman, T. Moffat, M. Pierce, A. Saha, P. Stetson, and D. Welch. We also thank the anonymous referee for making suggestions that improved this paper. G.R.M. was employed at the Anglo-Australian Observatory at the beginning of the this study and thanks its director, R. Cannon for his support. At ST ScI he was supported by NASA Grants Nos. NAG 5-1639 and NAGW-3138 and *HST* Grant No. GO-3591. G.M. was supported by NASA Contracts Nos. NAG 5-1611, NAS 7-918, and NAG 5-1620 while at the Space Astronomy Laboratory, University of Wisconsin-Madison when the spectral observations were taken. UKST IIIaJ survey films were employed in this study. A literature search was performed using NED, the NASA/IPAC Extragalactic Database, a facility operated by the Jet Propulsion Laboratory, Caltech, under contract with the National Aeronautics and Space Administration.

REFERENCES

Aaronson, M., Huchra, J., Mould, J., Schechter, P. L., & Tully, R. B. 1982, ApJ, 258, 64
Baldwin, J. A., Spinrad, H., & Terlevich, R. 1982, MNRAS, 198, 535
Becker, R., Mebold, U., Reif, K., & van Woerden, H. 1988, A&A, 203, 21
Bessell, M. S. 1979, PASP, 91, 589
Bica, E., Alloin, D., & Schmidt, A. 1990, MNRAS, 242, 241
Binggeli, B., & Cameron, L. M. 1991, A&A, 252, 27
Bothun, G. D., Mould, J. R., Caldwell, N., & MacGillivray, H. T. 1986, AJ, 92, 1007
Bottinelli, L., Gougenheim, L., Paturel, G., & de Vaucouleurs, G. 1983, A&A, 118, 4
Bottinelli, L., Gouguenheim, L., Fouqué, P., & Paturel, G. 1990, A&AS, 82, 391
Brinks, E., & Klein, U. 1988, 231, 63P
Burstein, D., & Heiles, C. 1984, ApJS, 54, 33
Burstein, D., Faber, S. M., Gaskill, C. M., & Krumm, N. 1984, ApJ, 287, 586
Caldwell, N., & Phillips, M. M. 1989, ApJ, 338, 789 (CP)
Cerviño, M., & Mas-Hesse, J. M. 1994, A&A (in press)
Corwin, Jr., H. G., de Vaucouleurs, A., & de Vaucouleurs, G. 1985, Southern Galaxy Catalogue (University of Texas Press, Austin, TX)
Deharveng, L., Caplan, J., & Lombard, J. 1992, A&AS, 94, 359
De Young, D. S., & Gallagher, J. S. 1990, ApJ, 356, L15
Dopita, M. A., & Evans, I. N. 1986, ApJ, 307, 431
Doyon, R., Joseph, R. D., & Wright, A. S. 1994, ApJ, 421, 101
Drinkwater, M., & Hardy, E. 1991, AJ, 101, 94
Fanelli, M. N., O'Connell, R. W., & Thuan, T. X. 1988, ApJ, 334, 665
Freeman, K. C. 1970, ApJ, 160, 811
Gallagher, J. S., & Hunter, D. A. 1987, AJ, 94, 43
Graham, J. A. 1982, PASP, 94, 244
Haro, G. 1956, Bol. Obs. Tonantzintla y Tacubaya, 14, 8
Heckman, T. M., & Leitherer, C. 1993, private communication
Howarth, I. D. 1983, MNRAS, 203, 301
Ichikawa, S.-I., Wakamatsu, K.-I., & Okamura, S. 1986, ApJS, 60, 475
IRAS Point Source Catalog 1988, *IRAS* Catalogs and Atlases, Vol. 2-6, (NASA, Washington, DC)
Johnson, H. L. 1966, ARA&A, 4, 193
Kennicutt, R. C. 1983, ApJ, 272, 54
Krienke, O. K., & Hodge, P. W. 1974, AJ, 79, 1242
Krüger, H., Fritze-von Alvensleben, U., Loose, H.-H., & Fricke, K. J. 1991, A&A, 242, 343
Kunth, D., Maurogordato, S., & Vigroux, L. 1988, A&A, 204, 10
Larson, R. 1988, in The Harlow-Shapley Symposium on Globular Cluster

Systems in Galaxies, IAU Symposium 126, edited by J. E. Grindlay and A. G. Davis Philip (Kluwer, Dordrecht), p. 311
Lauberts, A., & Sadler, E. 1984, A Compilation of *UBVRI* Photometry for Galaxies in the ESO/Uppsala Catalogue, ESO Scientific Report No. 3 (European Southern Observatory, Munich)
Longo, G., & de Vaucouleurs, A. 1983, A General Catalogue of Photoelectric Magnitudes and Colors in the *UBV* system of 3578 Galaxies Brighter than the 16-th *V*-Magnitude (1936–1983) (University of Texas Monographs in Astronomy, No. 3, Austin)
Loose, H.-H., & Thuan, T. X. 1985, in Star Forming Dwarf Galaxies and Related Objects, edited by D. Kunth, T. X. Thuan, and J. Tran Thanh Van (Editions Frontières, Paris), p. 73
Maeder, A., & Meynet, G. 1988, A&AS, 76, 411
Markarian, B. E. 1967, Astrofizika, 3, 55
Marlowe, A., Heckman, T., Wyse, R., & Schommer, R. 1994, ApJ (submitted)
Mas-Hesse, J. M., & Kunth, D. 1991, A&AS, 88, 399
McCall, M. L., Rybski, P. M., & Shields, G. A. 1985, ApJS, 57, 1
Meurer, G. R., Carignan, C., and Beaulieu, S. 1994, in preparation (Paper II)
Meurer, G. R., Freeman, K. C., Dopita, M. A., & Cacciari, C. 1992, AJ, 103, 60 (MFDC)
Osterbrock, D. E. 1989, Astrophysics of Gaseous Nebulae and Active Galactic Nuclei (University Science Books, Mill Valley, CA)
Peletier, R. F., Davies, R. L., Illingworth, G. D., Davis, L. E., & Cawson, M. 1990, AJ, 100, 1091
Peletier, R. F. 1993, A&A, 271, 51
Pierce, M. J., & Crabtree, D. R. 1993, New Perspectives on Stellar Pulsation and Pulsating Variable Stars, IAU Colloquium No. 139 (in press)
Price, J. S., & Gullixson, C. A. 1989, ApJ, 337, 658
Rieke, G. H., & Lebofsky, M. J. 1985, ApJ, 288, 618
Robinson, R. D., Sadler, E. M., Barton, J. R., & Straede, J. O. 1989, A Users Guide to the CCD Detectors at the AAT (Anglo-Australian Observatory Manual: AAO UM17.1.)
Sage, L. J., Salzer, J. J., Loose, H.-H., & Henkel, C. 1992, A&A, 265, 19
Salzer, J. J., MacAlpine, G. M., & Boroson, T. A. 1989, ApJS, 70, 447
Sandage, A., & Brucato, R. 1979, AJ, 84, 472
Sandage, A., Saha, A., Tamman, G. A., Labhardt, L., Schwengeler, H., Panagia, N., & Macchetto, F. P. 1994, ApJ, 423, L13
Schmidt, K.-H., & Boller, T. 1992, ANac, 313, 189
Searle, L., & Sargent, W. L. W. 1972, ApJ, 173, 25
Sérsic, J. L., Bajaja, E., & Colomb, R. 1977, A&A, 59, 19 (SBC)
Sérsic, J. L., & Donzelli, C. J. 1992, Ap&SS, 193, 87 (SD)
Stetson, P. B. 1987, PASP, 99, 191
Stone, R. P. 1977, ApJ, 218, 767
Struck-Marcell, C., & Tinsley, B. M. 1978, ApJ 221, 562
Thuan, T. X., & Martin, G. E. 1981, ApJ, 247, 823 (TM)
Thuan, T. X. 1987, in Nearly Normal Galaxies from the Planck Time to the Present, edited by S. M. Faber (Springer, New York), p. 67
Tonry, J., & Schneider, D. P. 1988, AJ, 96, 807
Vacca, W. D., & Conti, P. S. 1992, ApJ, 401, 543
Vader, J. P. 1986, ApJ, 305, 669
Viallefond, F., & Thuan, T. X. 1983, ApJ, 269, 444
Walsh, J. R., & Roy, J.-R. 1989, MNRAS, 239, 297
Wegner, G. 1979, Ap&SS, 60, 15
West, R. M. 1976, A&A, 53, 435

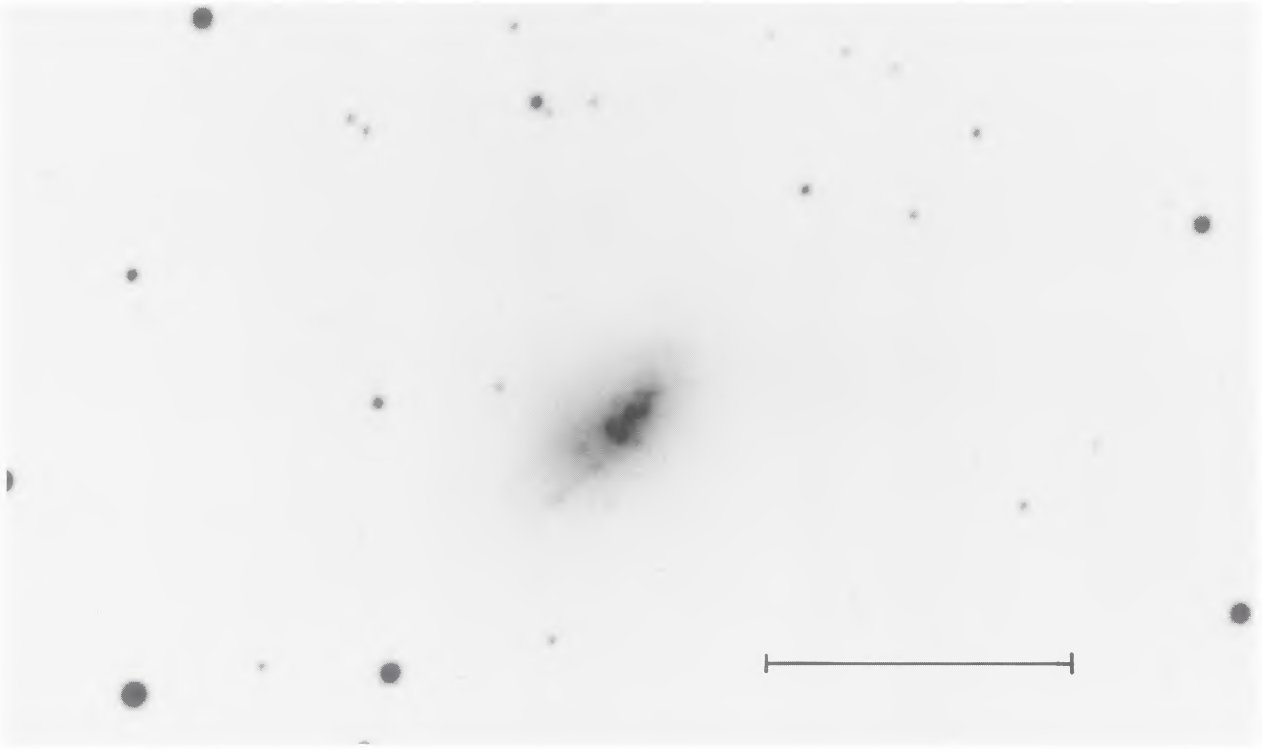

(a)

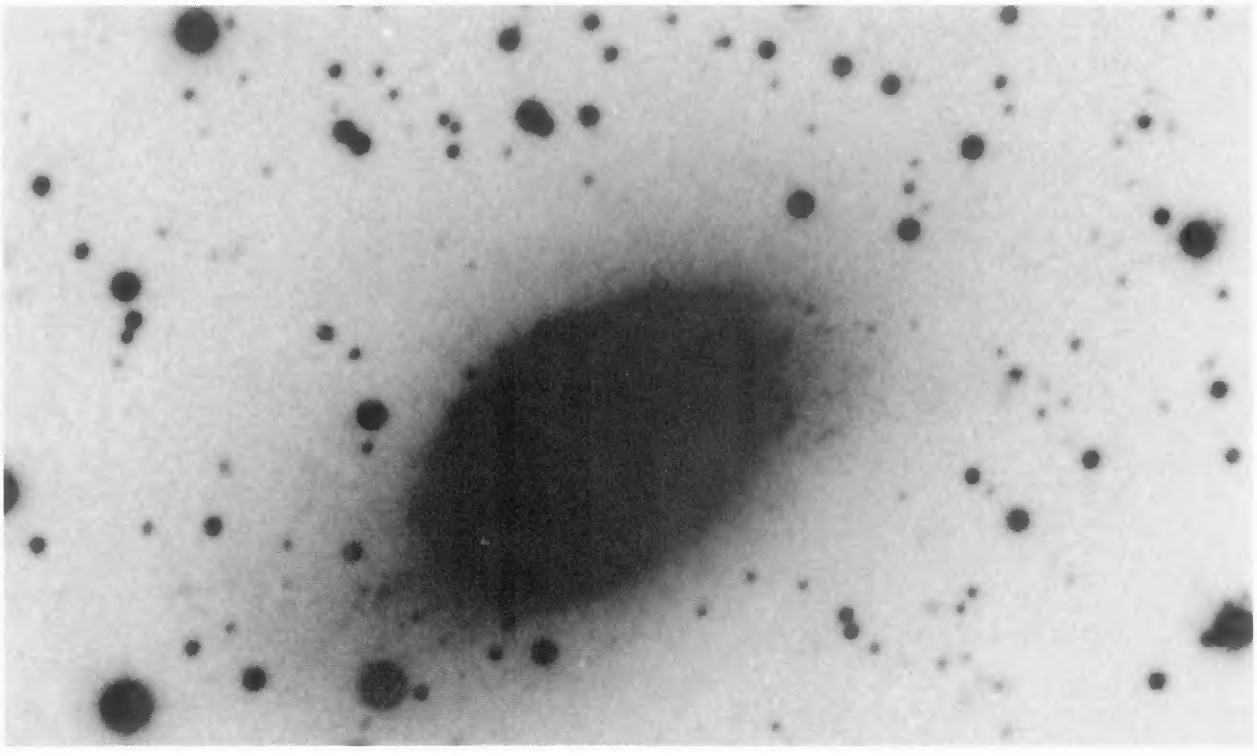

(b)

FIG. 1. Final *R* band image of NGC 2915. North is up, east to the left. The scale bar corresponds to 60″. Panel (a) is a low contrast image designed to show the full range of intensities from the sky value to those at the center of the galaxy. Panel (b) is a high contrast image highlighting the fainter structure.

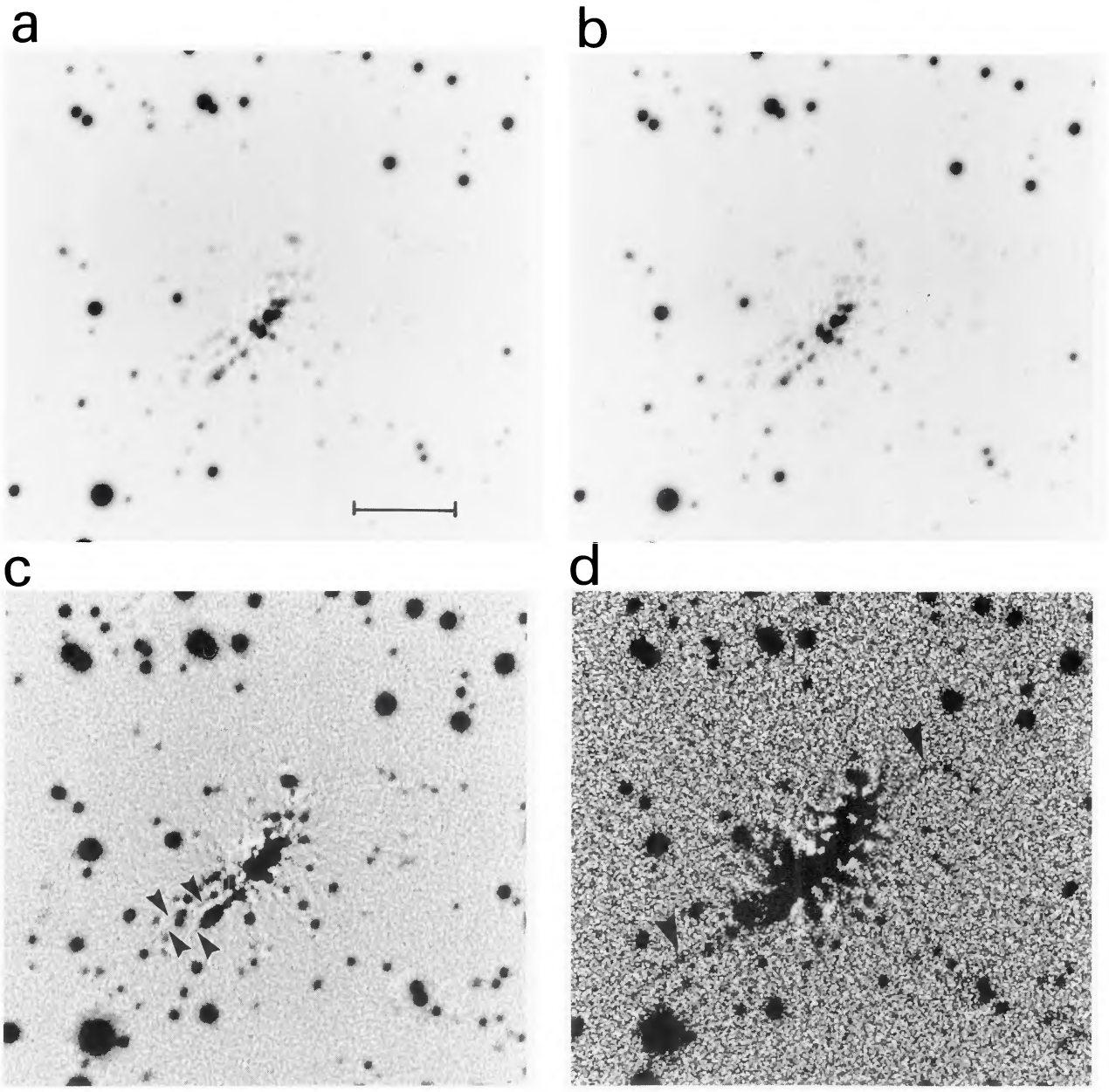

FIG. 2. The lumpy structure in NGC 2915. Orientation is the same as Fig. 1; the scale bar is 30″ long. (a) Shows the first iteration *R* band lumpy image. (b) Shows the final *R* band lumpy image. (c) Is a higher contrast version of (a). The faint wisps discussed in the text are indicated. (d) Is a *B* band lumpy image made like (a) except the smooth image was further smoothed with a 13×13 boxcar, before subtracting from the original image. The ejecta of SBC are marked.

Meurer *et al.* (see page 2023)

